crystals

MDPI

Article

Pt-Modified 3D NiCu Foam Catalysts for Enhanced Sodium Borohydride Electrooxidation

Žana Mickevičienė, Aldona Balčiūnaitė, Dijana Šimkūnaitė, Jūratė Vaičiūnienė, Loreta Tamašauskaitė-Tamašiūnaitė * and Eugenijus Norkus

Department of Catalysis, Center for Physical Sciences and Technology (FTMC), Sauletekio Ave. 3, LT-10257 Vilnius, Lithuania; zana.cinciene@ftmc.lt (Ž.M.); aldona.balciunaite@ftmc.lt (A.B.); dijana.simkunaite@ftmc.lt (D.Š.); jurate.vaiciuniene@ftmc.lt (J.V.); eugenijus.norkus@ftmc.lt (E.N.)
* Correspondence: loreta.tamasauskaite@ftmc.lt

Abstract

We report a straightforward and scalable strategy for the fabrication of three-dimensional Ni-rich bimetallic NiCu foam coatings on Ti substrates ($(NiCu)_{foam}/Ti$) via dynamic hydrogen bubble templating (DHBT) electrodeposition, followed by modification with an ultralow amount of Pt to construct an efficient ternary Ni–Cu–Pt catalytic system. The resulting foams exhibit highly porous dendritic architectures with interconnected channels, enabling a high density of electrochemically active sites and uniform metal distribution throughout the framework. Structural and compositional analyses (SEM–EDX) reveal a Ni-dominant composition (28.09–34.61 mg cm^{-2}), with significantly lower Cu content (2.47–4.16 mg cm^{-2}) and ultralow Pt loading (9.63–19.04 µg cm^{-2}), maximizing catalytic efficiency while minimizing noble metal usage. Electrochemical studies in alkaline media demonstrate that the NiCu foam possesses intrinsic borohydride electrooxidation activity, which is substantially enhanced upon Pt incorporation, delivering a threefold increase in activity compared to the unmodified foam and outperforming bulk Pt. This improvement is attributed to the synergistic interplay within the Ni-rich ternary system, where trace Pt acts as a highly effective promoter. When implemented as anodes in $NaBH_4$–H_2O_2 fuel cells, $Pt(NiCu)_{foam}/Ti$ achieves peak power densities of 239 and 301.6 mW cm^{-2} at 25 °C and 55 °C, respectively. Overall, this study presents a cost-effective and scalable route to high-performance electrocatalysts for alkaline direct borohydride fuel cells, significantly reducing reliance on noble metals while maintaining superior activity.

Keywords: nickel; copper; platinum; DHBT; sodium borohydride; oxidation; fuel cells

Check for updates

Academic Editors: Magdalena Laskowska and Agnieszka Karczmarska

Received: 2 April 2026
Revised: 22 April 2026
Accepted: 23 April 2026
Published: 24 April 2026

Copyright: © 2026 by the authors. Licensee MDPI, Basel, Switzerland. This article is an open access article distributed under the terms and conditions of the Creative Commons Attribution (CC BY) license.

1. Introduction

Fuel cells (FCs) represent a cornerstone of sustainable energy conversion technologies, offering the potential for high-efficiency, low-emission power generation for portable devices, electric vehicles, and stationary applications [1–4]. Among them, direct borohydride fuel cells (DBFCs) are particularly promising due to their use of sodium borohydride (e.g., KBH_4, $NaBH_4$) as a fuel, which exhibits high chemical stability in alkaline media and is solid at ambient conditions, facilitating storage and transport [5,6]. When paired with oxygen as the oxidant, $NaBH_4$–O_2 (DBFCs) can theoretically achieve a specific energy of 9.3 kW h kg^{-1} and a cell voltage of 1.64 V, surpassing those of conventional direct methanol (6.08 kW h kg^{-1}) and ethanol fuel cells (8.04 kW h kg^{-1}) [4,7–9]. Additionally, the borohydride oxidation reaction (BOR) produces metaborate ($NaBO_2$), a non-toxic byproduct that

can be recycled to regenerate $NaBH_4$, making DBFCs both environmentally friendly and potentially sustainable [3–5,9,10].

In alkaline media, the anodic BOR and cathodic oxygen reduction reaction (ORR) define the overall DBFC performance [5,6]:

$$BH_4^- + 8OH^- \rightarrow BO_2^- + 6H_2O + 8e^-,\ E_a^0 = -1.24\ \text{V vs. SHE} \quad (1)$$

$$O_2 + 2H_2O + 4\,e^- \rightarrow 4\,OH^-,\ E_c^0 = +0.40\ \text{V vs. SHE} \quad (2)$$

The overall reaction is as follows:

$$BH_4^- + 2O_2 \rightarrow BO_2^- + 2H_2O,\ E_{cell}^0 = 1.64\ \text{V} \quad (3)$$

Ideally, BOR involves an eight-electron transfer per $BH_4{}^-$ anion, but in practice this is hindered by side reactions such as non-faradaic hydrolysis and hydrogen evolution, which reduce faradaic efficiency and overall cell performance [8,11,12]. Therefore, careful design of anode catalysts is critical to maximize the selective oxidation of $BH_4{}^-$ while suppressing parasitic reactions.

Recently, hydrogen peroxide (H_2O_2) has been explored as an alternative oxidant to O_2 in DBFCs, forming direct borohydride–hydrogen peroxide fuel cells (DBHPFCs) [13,14]. The electroreduction in H_2O_2 at the cathode proceeds with faster kinetics and lower activation energy than O_2, resulting in higher theoretical cell voltages (up to 3.01 V) and specific energy (17 kW h kg^{-1}) [15–25]. In addition, H_2O_2 is a liquid, which simplifies storage, handling, and controlled feeding compared to gaseous O_2, offering practical advantages for compact, single-stack fuel cell systems. The reduction in H_2O_2 depends strongly on the electrolyte pH and can be described by the following reactions [23–25]:

$$\text{Alkaline medium}:\ 4HO_2^- + 4H_2O + 8e^- \rightarrow 12OH^-,\ E_c^0 = +0.87\ \text{V vs. SHE} \quad (4)$$

$$\text{Acidic medium}:\ 4H_2O_2 + 4H^+ + 8e^- \rightarrow 8H_2O,\ E_c^0 = +1.77\ \text{V vs. SHE} \quad (5)$$

Overall cell reactions:

$$\text{Alkaline medium}:\ BH_4^- + 4H_2O_2 \rightarrow BO_2^- + 6H_2O,\ E_{cell}^0 = 3.01\ \text{V} \quad (6)$$

$$\text{Acidic medium}:\ 4HO_2^- + BH_4^- \rightarrow 4OH^- + BO_2^- + 2H_2O,\ E_{cell}^0 = 2.11\ \text{V} \quad (7)$$

These reactions highlight the differences in thermodynamic behavior of H_2O_2 reduction in acidic and alkaline media. The higher standard reduction potential in acidic media (Equation (5), 1.77 V vs. SHE) compared to alkaline conditions (Equation (4), 0.87 V vs. SHE) reflects the direct involvement of protons in the cathodic reaction, enabling faster kinetics and higher theoretical cell voltages. Although borohydride is generally more stable in alkaline electrolytes, acidic media offer several advantages for fuel cell testing and operation: the increased driving force for H_2O_2 reduction can enhance cell performance, accelerate reaction rates at the cathode, and improve overall power output [6,12]. Therefore, while alkaline media suppress $BH_4{}^-$ hydrolysis, acidic electrolytes can provide superior electrochemical performance in practical DBHPFCs when carefully managed.

Despite these advantages, challenges remain, including the chemical decomposition of H_2O_2 and the parasitic hydrolysis of $NaBH_4$, both of which reduce energy efficiency and generate heat, ultimately limiting the practical performance of DBHPFC systems [17,18,23]:

$$NaBH_4 + 2H_2O \rightarrow NaBO_2 + 4H^+ + \text{heat} \quad (8)$$

$$2H_2O_2 \rightarrow 2H_2O + O_2 + \text{heat} \quad (9)$$

These issues are strongly dependent on the nature of the electrode materials, making the development of efficient and selective electrocatalysts a critical factor for improving overall fuel cell performance. In particular, catalysts must promote the complete electrooxidation of BH_4^- while suppressing undesired side reactions, such as hydrogen evolution and chemical hydrolysis, and simultaneously facilitate efficient H_2O_2 reduction at the cathode. Catalyst selection and electrode design play a crucial role in addressing these challenges [11,26–29]. Platinum-group metals (PGMs) remain the benchmark catalysts for borohydride oxidation due to their excellent activity and stability [3,11,22]. However, their high cost and limited availability significantly hinder large-scale commercialization. To address this limitation, significant efforts have been devoted to reducing noble metal loading by combining with transition or rare metals (Ni, Co, Cu, Mn, Zn) [20–22,25,30–37], or by dispersing small amounts of Pt nanoparticles onto high-surface-area support materials. Conventional porous supports include carbon-based materials (e.g., carbon black, graphite, carbon nanotubes, and mesoporous carbons) as well as metal–organic framework (MOF)-derived structures, which promote improved catalyst dispersion and utilization [11,26,38–40]. These materials offer high surface area, well-developed porosity, and good electrical conductivity, all of which are beneficial for electrocatalytic performance. However, their limited long-term stability, particularly under harsh electrochemical conditions, remains a significant challenge. Alternative support materials, including metal oxides, conductive polymers, and composite structures, have been explored to improve durability [34,41,42], with Ti-based oxide supports particularly attractive due to chemical stability and ability to prevent nanoparticle agglomeration or detachment from the surface [3,34].

In this context, nanostructured three-dimensional (3D) metal foams have emerged as promising self-supported electrodes, offering a viable alternative to conventional porous supports [43]. These materials provide high surface area, interconnected porosity, and excellent electrical conductivity, enabling efficient mass transport and electron transfer while maintaining structural integrity. Importantly, metal foams can serve simultaneously as both the catalyst support and a self-supporting conductive network, eliminating the need for binders or additional conductive additives and thereby simplifying electrode design. The preparation of MFs can be achieved through various techniques, ranging from non-electrochemical methods [44] to electrochemical techniques of selective dissolution, templating, and sol–gel methods [45]. A relatively new, yet very promising method of preparing metal foams is DHBT electrodeposition [46]. At present, most three-dimensional (3D) metal foams prepared via the DHBT method are based on monometallic systems, particularly Cu or Ni. These materials have attracted significant attention for electrochemical energy conversion applications [47], including supercapacitors [48,49], fuel cells [50], BOR [51], and water-splitting reactions such as the hydrogen evolution reaction (HER) and oxygen evolution reaction (OER) [52–56]. Their high surface area, interconnected porosity, and excellent electrical conductivity make them versatile platforms for electrocatalysis. However, their catalytic activity is inherently limited by the properties of a single-metal functionality. In contrast, bimetallic systems offer opportunities to tailor electronic structure and surface reactivity, leading to enhanced catalytic activity and selectivity. Among these, Ni–Cu systems are particularly attractive for borohydride electrooxidation due to their low cost, abundance, and favorable electrochemical properties. In addition, Ni provides intrinsic catalytic activity in alkaline media, while Cu can modify the electronic structure of Ni and improve selectivity by suppressing side reactions such as hydrogen evolution and borohydride hydrolysis [57–60]. However, most Ni–Cu catalysts have been prepared via conventional electrodeposition [57–64], which typically produces dense films or nanoparticles with limited surface area and restricted mass transport. In contrast, DHBT enables the

formation of highly porous, three-dimensional Ni–Cu foams via in situ hydrogen bubble generation, offering increased active surface area and improved reactant accessibility by creating self-supported architectures without binders, making DHBT particularly suitable for high-performance electrocatalysis [46]. Despite this potential, bimetallic Ni–Cu foams prepared via DHBT remain relatively underexplored, particularly for sodium borohydride electrooxidation therefore represents a promising yet insufficiently explored direction.

Beyond bimetallic design, the incorporation of small amounts of noble metals provides an additional strategy to enhance catalytic performance. In particular, ultralow Pt loading can act as a promoter by facilitating the oxidation of reaction intermediates while minimizing cost. While bimetallic and trimetallic catalysts supported on monometallic Ni foams have been widely investigated for sodium borohydride electrooxidation [16–18,51,65,66], these approaches still rely on pre-formed monometallic substrates. In contrast, the development of trimetallic systems based on DHBT-derived bimetallic NiCu foams remain largely unexplored, especially under conditions of ultralow noble metal loading.

In this study, we present a straightforward and scalable strategy for fabricating an advanced and cost-effective Ni-rich bimetallic NiCu foam catalyst supported on a titanium (Ti) substrate ($(NiCu)_{foam}/Ti$) via DHBT electrodeposition, followed by modification with trace amounts of Pt to construct a ternary $Pt(NiCu)_{foam}/Ti$ system. Unlike the widely studied monometallic Ni or Cu foams, this study introduces a Ni-rich bimetallic Ni–Cu foam synthesized via DHBT, providing a synergistic platform that combines the intrinsic activity of Ni with the selectivity-modifying role of Cu. The resulting architecture features a three-dimensional porous Ni–Cu framework with interconnected porosity. Furthermore, the incorporation of ultralow Pt loading enables the construction of a highly efficient ternary systems, significantly outperforming both monometallic foams and bulk Pt while drastically reducing noble metal usage. The deposition parameters, including NiCu deposition time, were optimized to tailor morphology and composition for sodium borohydride electrooxidation. The developed $(NiCu)_{foam}/Ti$ and $Pt(NiCu)_{foam}/Ti$ catalysts were evaluated both for BOR and as anodes in $NaBH_4$–H_2O_2 fuel cells, demonstrating a practical, scalable, and economically viable approach to high-performance borohydride-based energy conversion. Overall, this study highlights the potential of integrating advanced three-dimensional electrode architectures with minimal noble metal loading to achieve efficient and scalable fuel cell technologies.

2. Materials and Methods

2.1. Chemicals

Analytical-grade reagents were used throughout this study without any additional purification. The following reagents were purchased from Sigma-Aldrich (Saint Louis, MO, USA): titanium (Ti) foil (99.7% purity), sodium borohydride ($NaBH_4$, 99.9%, 96 wt.%), copper(II) sulfate pentahydrate ($CuSO_4 \cdot 5H_2O$, 98%), and nickel(II) sulfate hexahydrate ($NiSO_4 \cdot 6H_2O$, 99%). Hexachloroplatinic acid (H_2PtCl_6, 99.95%) was purchased from Alfa Aesar (Ward Hill, MA, USA). Sodium hydroxide (NaOH, 98.8%), sulfuric acid (H_2SO_4, 96%), and hydrochloric acid (HCl, 35–38%) were obtained from Chempur (Piekary Śląskie, Poland). All aqueous solutions were prepared using deionized water obtained from a Millipore Elix 3 (Millipore SAS, Molsheim, France) purification system.

2.2. Preparation of NiCu Foams and $Pt(NiCu)_{foam}$/Ti Catalysts

Ti plates with a geometric surface area of 2 cm^2 were utilized as substrates for the fabrication of NiCu foams. The Ti plates were degreased with acetone and then pretreated in a concentrated sulfuric acid solution at 40 °C for 3 s. Afterward, the plates were rinsed thoroughly with deionized water and air-dried. NiCu foam layers were electrodeposited

onto the Ti surface using a galvanostatic method at a constant current of 1.5 A cm^{-2} for durations of 3, 6, or 9 min. The resulting catalysts were labeled $(NiCu)_{foam}$/Ti-1, $(NiCu)_{foam}$/Ti-2, and $(NiCu)_{foam}$/Ti-3, respectively. The plating solution, prepared at room temperature (25 °C), contained 0.5 M $NiSO_4$, 0.01 M $CuSO_4$, 1.5 M H_2SO_4, and 1 M HCl. For comparison, pure Ni or Cu layers were deposited on the Ti surface. The Pt-modified catalysts $(Pt(NiCu)_{foam}/Ti)$ were obtained by immersing the NiCu-coated Ti electrodes in a solution containing 1 mM H_2PtCl_6 and 0.1 M HCl at 25 °C for 1 min. The resulting catalysts were then rinsed with deionized water and air-dried.

2.3. Surface Characterization of Catalysts

The morphology and composition of the fabricated catalysts were characterized using a Hitachi Ltd., TM4000Plus SEM workstation (Tokyo, Japan). The samples were mounted on aluminum stubs with conductive carbon tape. SEM imaging was done in high-vacuum mode at an accelerating voltage of 15 kV, a working distance of 9.7 ± 0.2 mm, and at different magnifications. The BSE (backscattered electrons) detector was used for the samples. An Oxford Instruments AZtecOne EDS system (High Wycombe, UK) was used for elemental analysis at an accelerating voltage of 15 kV with a live time of 60 s. The analysis encompassed a total of three SEM images captured from three distinct regions. The reported composition of the catalysts represents their average composition. The metal loading in the catalysts was estimated by employing Inductively Coupled Plasma Optical Emission Spectroscopy (ICP-OES). The ICP-OES spectra were recorded using an Optima 7000DV spectrometer (Perkin Elmer, Waltham, MA, USA) at the following wavelengths: Ni—231.604 nm, Cu—327.393 nm, and Pt—265.945 nm.

2.4. Electrochemical Measurements

Electrochemical measurements were conducted using a PGSTAT100 potentiostat (Metrohm Autolab B.V., Utrecht, The Netherlands) controlled via NOVA software (version 1.6.013). BOR studies were performed in a thermostated, three-electrode electrochemical cell. The $(NiCu)_{foam}$/Ti and $Pt(NiCu)_{foam}$/Ti catalysts served as the working electrodes. A platinum sheet (1.0 × 1.0 cm) was used as the counter electrode. An Ag/AgCl (3.0 M KCl) reference electrode was coupled to the working electrolyte via a salt bridge with a Luggin capillary, thereby minimizing direct exposure of the reference electrode to the alkaline solution and reducing the risk of chloride contamination [67]. The stability of the Ag/AgCl electrode was independently evaluated before and after the electrochemical experiments using the $Fe(CN)_6^{3-}/^{4-}$ redox couple. Cyclic voltammetry showed that the midpoint potential ($E_{1/2}$) varied by less than 5 mV, within instrumental uncertainty, indicating negligible reference electrode drift and ensuring the reliability of the electrochemical measurements [68,69]. The electrocatalytic activity of the prepared catalysts was evaluated by recording cyclic voltammograms (CVs) in a background 1 M NaOH solution and 0.05 M $NaBH_4$ + 1 M NaOH solution. Measurements were performed within a potential window ranging from −1.2 V to +0.6 V vs. Ag/AgCl at a scan rate of 10 mV s^{-1}. All electrolyte solutions were thoroughly deaerated by purging with argon (Ar) prior to the electrochemical tests.

2.5. Fuel Cell Tests

DBHPFCs tests were conducted using $(NiCu)_{foam}$/Ti and $Pt(NiCu)_{foam}$/Ti electrodes with a geometric area of 2 cm^2 as the anode, while a Pt sheet served as the cathode. The anolyte consisted of an alkaline solution containing 1 M $NaBH_4$ and 4 M NaOH, whereas the catholyte comprised 5 M H_2O_2 and 1.5 M HCl. Each compartment of the cell was filled with 100 mL of the respective aqueous electrolyte. To minimize H_2O_2 decomposition and prevent BH_4^- loss through hydrolysis during storage, all test solutions

were freshly prepared immediately prior to measurements. A Nafion N117 membrane was employed to separate the anodic and cathodic compartments of the single direct $NaBH_4$–H_2O_2 fuel cell. The reported current densities were normalized to the geometric area of the catalysts. All electrochemical measurements were performed using a Zennium electrochemical workstation (ZAHNER-Elektrik GmbH & Co. KG, Kronah, Germany). Fuel cell performance was evaluated by recording polarization curves and deriving the corresponding power density curves.

3. Results

3.1. Morphology and Composition of $(NiCu)_{foam}$/Ti and $Pt(NiCu)_{foam}$/Ti

Figure 1 presents representative SEM images of NiCu and Pt(NiCu) metallic foams electrodeposited on Ti substrates at a current density of 1.5 A cm^{-2} for deposition times of 3, 6, and 9 min. All samples exhibit a highly porous three-dimensional architecture composed of randomly distributed, interconnected macropores with dendritic pore walls. The formation of the Ni–Cu foam structure originates from the DHBT mechanism occurring at high cathodic current densities, where hydrogen evolution generates bubbles that act as transient templates during metal deposition. Metal growth occurs in the regions between bubbles, while bubble coalescence and detachment generate the interconnected meso- and macroporous network. The NiCu deposits obtained after 3 min deposition (Figure 1a) exhibits a high density of relatively small interconnected pores. Increasing the deposition time to 6 and 9 min (Figure 1b,c) leads to progressive enlargement of the pore diameter from approximately 10 μm to several tens of micrometers, accompanied by a decrease in pore density. This evolution reflects structural coarsening and thickening of the dendritic framework as deposition proceeds.

After Pt modification via galvanic displacement (Figure 1a‘–c‘), the overall foam morphology remains preserved. However, the dendritic framework becomes more pronounced, exhibiting a fern-like structure with secondary and tertiary branching. Consequently, the pore walls become less compact and display increased surface roughness. The hierarchical porosity of the foams thus arises from both the macroporous architecture and the open dendritic walls, providing a highly accessible hierarchical porous structure.

Although distinct Pt surface species cannot be clearly resolved in the SEM images (Figure 1a‘–c‘), ICP–OES analysis confirms successful Pt incorporation in all modified samples (Table 1).

Table 1. The composition of catalysts determined by ICP-OES analysis.

Sample	Ni Loading, mg_{Ni} cm^{-2}	Cu Loading, mg_{Cu} cm^{-2}	Pt Loading, μg_{Pt} cm^{-2}	Total Loading, mg cm^{-2}
$(NiCu)_{foam}$/Ti-1	28.09	2.47	-	30.56
$(NiCu)_{foam}$/Ti-2	30.11	2.84	-	32.95
$(NiCu)_{foam}$/Ti-3	34.61	4.16	-	38.77
$Pt(NiCu)_{foam}$/Ti-1	9.98	1.14	9.63	11.13
$Pt(NiCu)_{foam}$/Ti-2	12.41	2.52	13.79	14.94
$Pt(NiCu)_{foam}$/Ti-3	22.11	2.91	19.04	25.04

The data reveal a clear deposition-time dependence: for the unmodified $(NiCu)_{foam}$/Ti electrodes, the Ni loading increases from 28.09 to 30.11 and 34.61 mg cm^{-2} as the deposition time increases from 3 to 6 and 9 min, respectively, while the Cu loading increases from 2.47 to 2.84 and 4.16 mg cm^{-2}. This systematic metal accumulation is consistent with the observed thickening of the dendritic framework. After Pt modification, Pt loadings also increase monotonically with deposition time, reaching 9.63, 13.79, and 19.04 μg cm^{-2} for

NiCu foams deposited for 3, 6, and 9 min, respectively. The trend indicates that more developed NiCu foams provide a larger effective surface area for galvanic displacement, enhancing Pt incorporation.

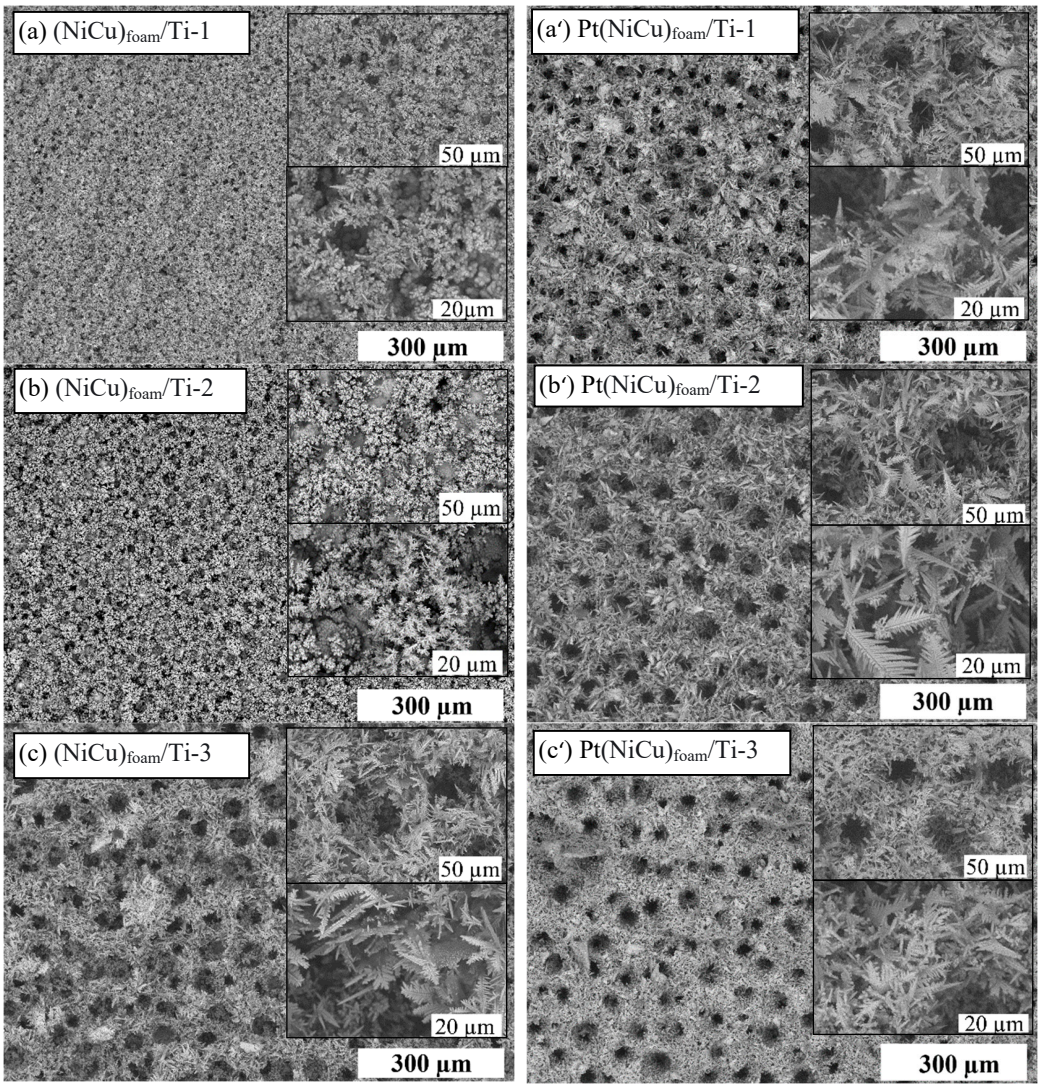


Figure 1. SEM images of $(NiCu)_{foam}$/Ti (**a**–**c**) and $Pt(NiCu)_{foam}$/Ti (**a′**–**c′**). The $(NiCu)_{foam}$ layers were deposited on the Ti surface at a current density of 1.5 A cm^{-2} for different deposition times: 3 min (**a**,**a′**), 6 min (**b**,**b′**), and 9 min (**c**,**c′**). The Pt deposition time was 1 min. The insets show the corresponding SEM images at higher magnification.

Notably, the total catalyst loading of $Pt(NiCu)_{foam}$/Ti (11.13–25.04 mg cm^{-2}) is significantly lower than that of the corresponding unmodified $(NiCu)_{foam}$/Ti electrodes (30.56–38.77 mg cm^{-2}), indicating partial Ni dissolution during the displacement process. This suggests that Pt incorporation occurs via a surface exchange mechanism, involving simultaneous Ni dissolution and Pt deposition rather than simple metal accumulation. Despite this partial mass loss, Ni remains the dominant metallic component, while Cu is largely retained within the framework. The observed decrease in Ni loading after the Pt modification step (from 34.61 to 22.11 mg cm^{-2}) is associated with the galvanic displacement mechanism used to introduce Pt onto the NiCu foam surface. In this process, surface Ni atoms are partially oxidized and dissolved as Ni^{2+} while Pt is simultaneously reduced and deposited from the H_2PtCl_6/HCl solution [70]. Therefore, the reduction in Ni content does not indicate structural collapse of the foam, but rather reflects a surface-limited redox exchange process intrinsic to galvanic replacement. Importantly, the amount of Pt

introduced is extremely low (19.04 μg cm^{-2}), remaining approximately three orders of magnitude lower than the residual Ni content (22.11 mg cm^{-2}). This large difference confirms that Pt incorporation occurs predominantly at the surface level, leading to catalytic surface modification rather than bulk compositional reconstruction. Despite partial Ni dissolution, the hierarchical three-dimensional foam architecture remains fully preserved, as confirmed by SEM analysis (Figure 1), which shows no evidence of framework collapse or loss of structural integrity after Pt modification. The dendritic morphology and interconnected porous network are maintained, indicating that the galvanic displacement process affects only a superficial region of the NiCu framework.

Further insight from the elemental mapping by EDX (Figure 2) reveals a uniform distribution of Ni and Cu throughout the dendritic framework, confirming successful co-deposition without detectable elemental segregation.

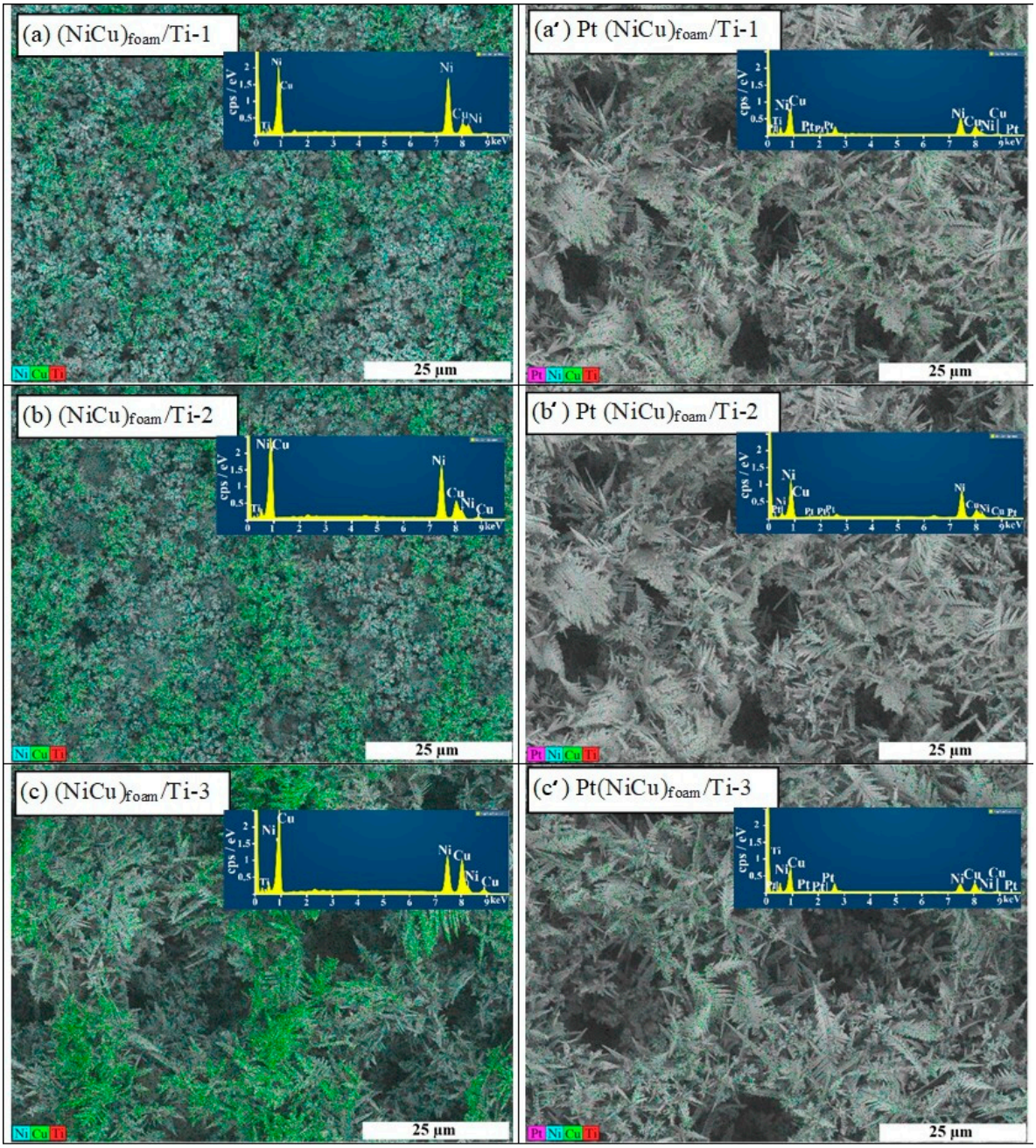


Figure 2. Elemental mapping and the corresponding EDX spectra (the insets) of $(NiCu)_{foam}$/Ti (**a**–**c**) and $Pt(NiCu)_{foam}$/Ti (**a′**–**c′**) catalysts as depicted in Figure 1.

After Pt modification, characteristic Pt signals appear in the spectra, and the corresponding elemental maps show homogeneous Pt dispersion over the foam surface. No localized Pt-rich domains or large agglomerates are observed within the resolution of SEM–EDX analysis, indicating that Pt is likely present as finely dispersed surface species decorating the dendritic branches. Such dispersion maximizes interfacial contact between Pt and the NiCu substrate, which may promote electronic interactions and enhance catalytic activity. At the same time, although the porous and dendritic structure improves surface accessibility, its quantitative contribution cannot be reliably determined due to the absence of a well-defined non-faradaic region for capacitance-based analysis in this system.

3.2. Electrochemical Behavior of Ni/Ti, Cu/Ti and $(NiCu)_{foam}$/Ti

The electrochemical properties of the $(NiCu)_{foam}$/Ti and $Pt(NiCu)_{foam}$/Ti catalysts were investigated by cyclic voltammetry in 1.0 M NaOH with and without 0.05 M $NaBH_4$ (Figures 3–6). For comparison, the electrochemical behavior of the pure Cu/Ti and Ni/Ti electrodes was also examined and systematically compared with that of the NiCu foam and Pt-modified NiCu foam catalysts toward sodium borohydride electrooxidation and in the supporting 1.0 M NaOH electrolyte. The CV of the pure Cu/Ti electrode (Figure 3a) shows typical oxidation processes in alkaline solution associated with the formation of Cu(I) and Cu(II) species including, Cu_2O, CuO, and $Cu(OH)_2$ [71–73]. During the anodic scan, two peaks (a1 and a2) are observed, corresponding to the sequential oxidation steps: $Cu \rightarrow Cu_2O$ and $Cu_2O \rightarrow CuO/Cu(OH)_2$. In the reverse scan, the corresponding cathodic peaks (c1 and c2) represent the stepwise reduction in these oxide species, either $CuO \rightarrow Cu_2O$ (c1) and $Cu_2O \rightarrow Cu^0$ (c2) [73], or the direct reduction in CuO and $Cu(OH)_2$ to metallic Cu [72,73].

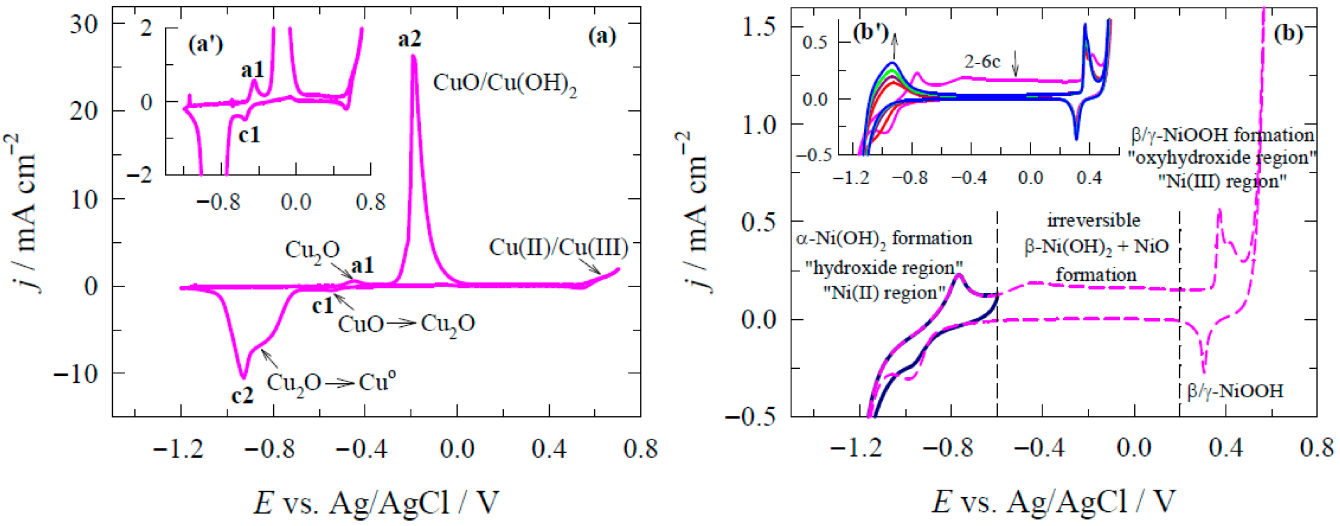


Figure 3. CVs of Cu/Ti (**a**) and Ni/Ti (**b**) catalysts recorded in 1 M NaOH at a scan rate of 10 mV s^{-1}. The inset (**a'**) represents the CV at higher magnification. The inset (**b'**) represents corresponding CVs of Ni/Ti catalyst with a different number of cycles.

The CV of the freshly prepared Ni/Ti electrode in 1.0 M NaOH (Figure 3b) displays characteristic features related to the formation of nickel hydroxide and oxyhydroxide species [74–76]. In the potential range from −1.2 to −0.6 V, metallic Ni is reversibly oxidized to surface α-$Ni(OH)_2$ during the anodic sweep and reduced back to Ni^0 during the cathodic sweep, as shown by the first scan (blue curve). At more positive potentials (−0.6 to −0.2 V), α-$Ni(OH)_2$ irreversibly transforms into the more stable β-$Ni(OH)_2$ phase and/or NiO [74].

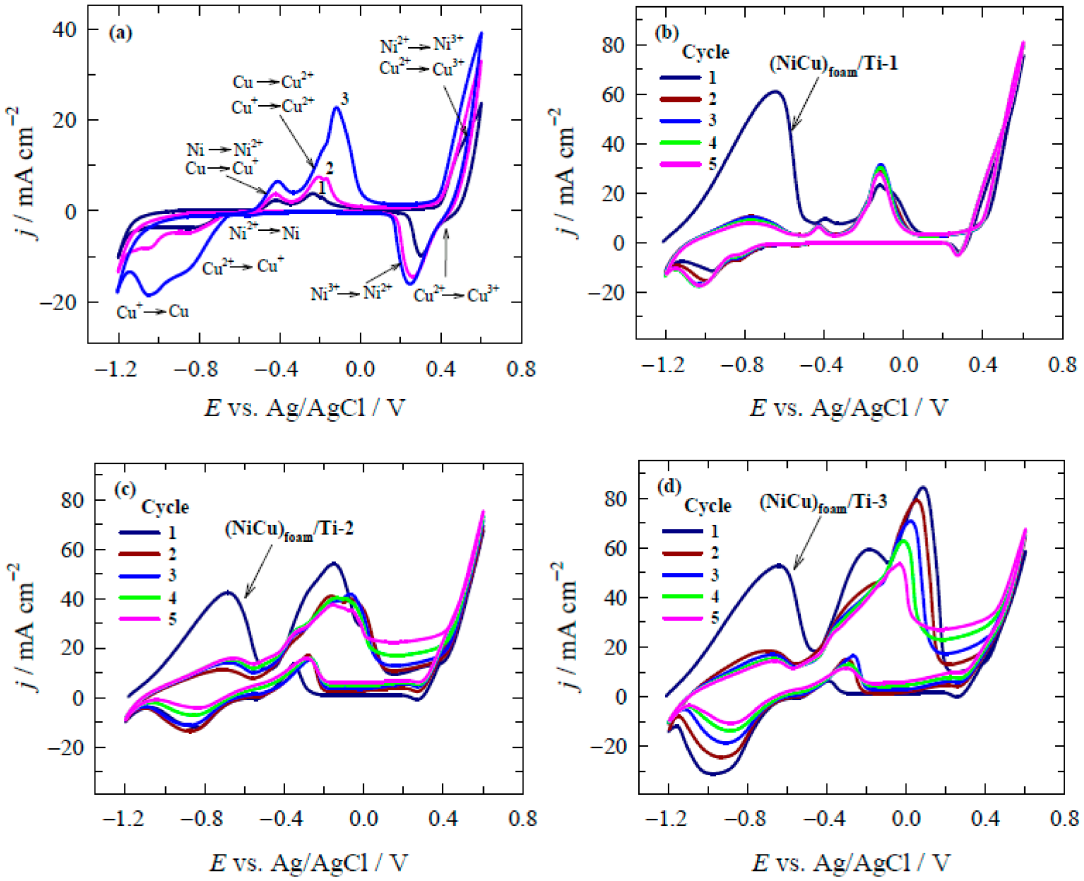


Figure 4. CVs of $(NiCu)_{foam}$/Ti catalysts: (**a**) CVs recorded in 1 M NaOH at a scan rate of 10 mV s^{-1} for samples prepared with deposition times of 3 min – (1), 6 min – (2), and 9 min – (3); (**b**–**d**) CVs of the same catalysts recorded in 0.05 M $NaBH_4$ + 1 M NaOH at a scan rate of 10 mV s^{-1}.

Further anodic polarization (−0.2 to +0.6 V) induces the formation of NiOOH through the Ni^{2+}/Ni^{3+} redox transition, producing a well-defined peak pair centered near +0.35 V. Repeated cycling gradually stabilizes the oxidized nickel surface, as evidenced by the evolution of the voltammetric features shown in the inset of Figure 3. The diminishing α-$Ni(OH)_2$ features and the appearance of an anodic peak at more negative potentials (approximately at −0.8 V vs. −0.6 V) indicate progressive surface oxidation and passivation, consistent with previous reports [76,77].

These observations confirm that both Ni and Cu undergo redox transformations in alkaline media, providing the electrochemical basis for the more complex behavior observed for the bimetallic $(NiCu)_{foam}$/Ti and ternary $Pt(NiCu)_{foam}$/Ti catalysts.

The electrochemical behavior of the $(NiCu)_{foam}$/Ti catalysts, deposited for 3, 6, and 9 min, in 1 M NaOH solution and that containing 0.05 M $NaBH_4$ is shown in Figure 4. In the absence of sodium borohydride (Figure 4a), the voltammograms exhibit broad anodic and cathodic features characteristic of overlapping Ni and Cu redox processes in alkaline media [76,77]. At low potentials, metallic Ni and Cu are oxidized to Ni(II) and Cu(I)/Cu(II), while further anodic polarization generates Ni(III) oxyhydroxide (NiOOH) and highly oxidized Cu species, possibly including Cu(III)-like hydroxide/oxyhydroxide surface species [72,73]. The broad anodic features between approximately −0.6 and +0.2 V can be attributed to overlapping Ni(II)/Ni(III) and Cu-related redox transitions.

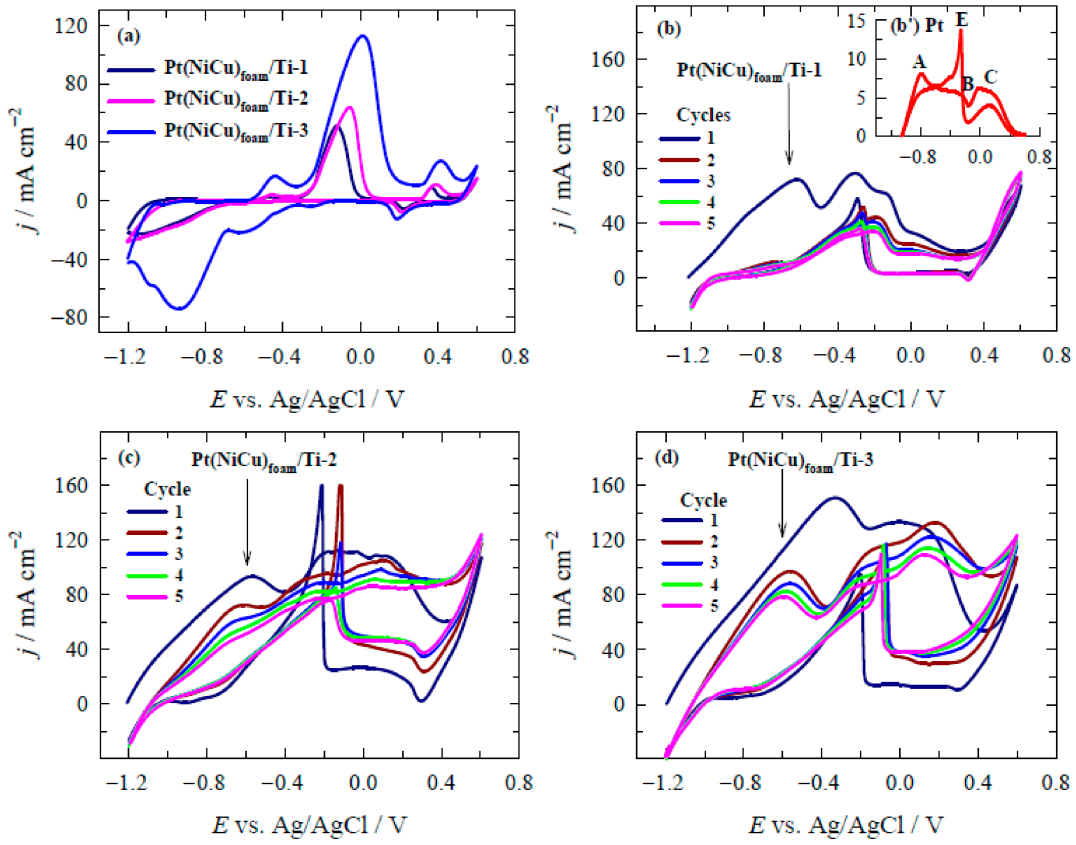


Figure 5. CVs of $Pt(NiCu)_{foam}/Ti$ catalysts: (**a**) CVs recorded in 1 M NaOH at 10 mV s^{-1} for samples prepared with CuNi foams deposition times of 3 min – (1), 6 min – (2), and 9 min – (3); (**b**–**d**) CVs of the same catalysts recorded in 0.05 M $NaBH_4$ + 1 M NaOH at a scan rate of 10 mV s^{-1}. The inset (**b'**) presents CV of Pt in 0.05 M $NaBH_4$ + 1 M NaOH at 10 mV s^{-1}.

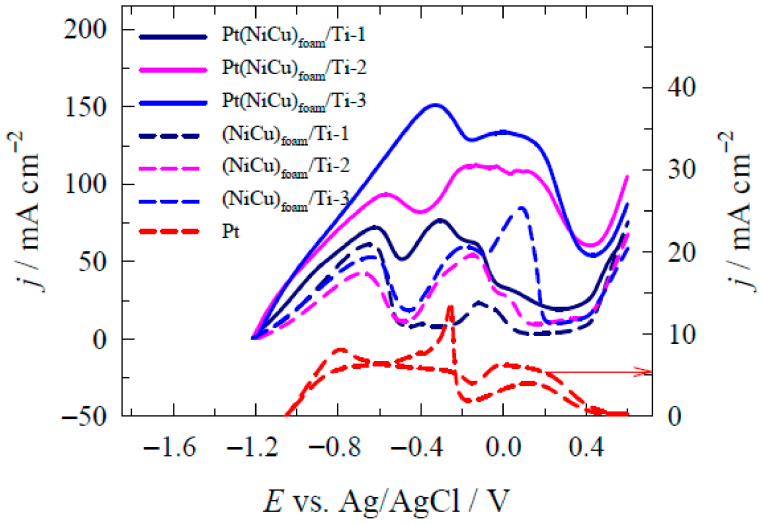


Figure 6. First positive-potential going scans of Pt (long dashed lines), different $(NiCu)_{foam}/Ti$ (dotted lines) and $Pt(NiCu)_{foam}/Ti$ (solid lines) catalysts, recorded in 0.05 M $NaBH_4$ + 1 M NaOH at a scan rate of 10 mV s^{-1}.

With increasing deposition time metal loading increases, resulting in higher current densities (Figure 4a). Specifically, the Ni loading rises from 28.09 to 30.11 and 34.61 mg cm^{-2} and Cu from 2.47 to 2.84 and 4.16 mg cm^{-2} for deposition times of 3, 6 and 9 min, respectively. The higher metal content enhances the density of electrochemically accessible catalytic sites within the three-dimensional NiCu foam architecture, which

creates a more porous and conductive network for electrochemical reactions [58]. However, it should be noted that a quantitative determination of electrochemically active surface area (ECSA) is not straightforward in this system due to overlapping faradaic processes associated with Ni and Cu redox transitions in alkaline media [74,78–81]. Consequently, longer deposition times correlate with higher current densities, reflecting more efficient utilization of the NiCu surface.

In the presence of borohydride (Figure 4b–d), the voltammograms changes markedly, confirming catalytic electrooxidation of BH_4^- on the electrode surface. The catalytic activity strongly depends on both the catalysts loading and the redox state of Ni. During the first cycle, a pronounced anodic peak near −0.65 V is observed, which can be attributed to borohydride electrooxidation on freshly exposed metallic Ni sites, where adsorption and activation of BH_4^- occur efficiently [8,58,59,82,83].

Repeated cycling gradually reduces the current due to the formation of Ni (hydr)oxide layers and partial surface blocking by reaction intermediates. A similar response observed is observed in the background electrolyte (Figure 3a', inset). It indicates that irreversible Ni oxidation contributes significantly to this decrease, reducing the number of metallic sites available for borohydride adsorption. At more positive potentials, the Ni^{2+}/Ni^{3+} redox transition becomes active, forming NiOOH species, which can promote the electrooxidation of borohydride intermediates via a redox-mediated pathway. Thus, despite progressive surface oxidation and intermediate accumulation, the catalyst retains substantial activity due to the continued involvement of NiOOH in the oxidation process.

Cu incorporation within the NiCu foam additionally affects the catalytic behavior. Cu enhances BOR selectivity relative to competing reactions (e.g., hydrogen evolution, borohydride hydrolysis) and stabilizes Ni active sites against oxidation [59,60,62]. In addition, the formation of soluble copper hydroxide species (e.g., $[Cu(OH)_4]^{2-}$) in strongly alkaline media, may further influence long-term stability by intermittently exposing underlying Ni active sites, thereby helping to preserve catalytic activity [59,72,73]. Overall, the electrocatalytic performance of $(NiCu)_{foam}/Ti$ arises from the synergistic interplay between metallic Ni sites responsible for BH_4^- activation, the redox-mediated catalytic activity of $NiOOH/Ni(OH)_2$, and Cu-induced modifications that enhance surface reactivity. Along with these factors, catalyst loading and the open 3D foam architecture modulate active site accessibility, stability, and utilization, supporting sustained performance during repeated cycles. It is important to note that, in contrast to many noble-metal systems, the determination of double-layer capacitance (C_{dl}) and electrochemically active surface area (ECSA) for Ni–Cu-based electrodes in alkaline media is inherently challenging. As shown in Figure 4a, the entire investigated potential window is dominated by overlapping faradaic processes, including $Ni(OH)_2/NiOOH$ and $Cu^0/Cu^+/Cu^{2+}$ transitions. These contributions extend across a broad potential range, making it difficult to identify a purely non-faradaic region suitable for reliable C_{dl} extraction. As a result, any capacitance-derived ECSA would include significant pseudo-capacitive contributions and may lead to overestimation of the true surface area. Therefore, in this work, the role of surface area is discussed qualitatively based on morphological evolution (SEM, Figure 1), compositional analysis (Table 1), and corresponding electrochemical trends, while avoiding potentially misleading quantitative estimates.

3.3. Effect of Pt Modification on $(NiCu)_{foam}/Ti$

Modification of (NiCu)foam/Ti with ultralow Pt loadings (9.63, 13.79, and 19.04 μg_{Pt} cm^{-2}, corresponding to 3, 6, and 9 min NiCu deposition, respectively) substantially enhances current densities in both 1 M NaOH and borohydride-containing electrolytes (Figure 5). In the base electrolyte (Figure 5a), weak cathodic peak near

−0.3 V is attributed to the reduction in Pt oxides formed during the anodic scan at potentials more positive than −0.2 V, confirming the presence of Pt nanoparticles on the foam surface. Peaks in the range of 0.2–0.4 V correspond to the reversible Ni(II)/Ni(III) transition:

$$Ni(OH)_2 + OH^- \rightleftharpoons NiOOH + H_2O + e^- \quad (10)$$

For comparison, a typical CV of bulk Pt recorded in a borohydride-containing electrolyte is shown in Figure 5b (inset). Two well-defined anodic peaks A and C are observed. Peak A (at approximately −0.8 V) is typically assigned to the oxidation of hydrogen (Equation (12)), produced via the catalytic hydrolysis of sodium borohydride (Equation (11)) [37]:

$$BH_4^- + H_2O \rightarrow BH_3(OH)^- + H_2 \quad (11)$$

$$H_2 + 2OH^- \rightarrow 2H_2O + 2e^- \quad (12)$$

A less intense peak B (at approximately −0.2 V) is assigned to the electrooxidation of $BH_3(OH)^-$ intermediates:

$$BH_3(OH)^- + 3OH^- \rightarrow BO_2^- + 3/2\ H_2 + 2H_2O + 3e^- \quad (13)$$

Peak C (0–0.2 V) corresponds to direct borohydride electrooxidation:

$$BH_4^- + 8OH^- \rightarrow BO_2^- + 6H_2O + 8e^- \quad (14)$$

During the reverse scan, a sharp peak E near −0.3 V is attributed to the electrooxidation of $BH_3(OH)^-$ intermediates on partially oxidized Pt surfaces. In contrast to bulk Pt (Figure 5b', inset), CV analysis reveals that the $Pt(NiCu)_{foam}/Ti$ electrodes exhibit multiple anodic features and current densities several tens of times higher than bulk Pt under identical conditions. Notably, hydrogen-related features typically observed on Pt near −0.8 V are attenuated, while the dominant anodic feature appears near −0.6 V. This behavior resembles that observed for unmodified $(NiCu)_{foam}/Ti$ (Figures 4 and 6) and is consistent with previous reports for Pt–Ni-based catalysts [33]. The attenuation of hydrogen-related features indicates a reduced contribution from hydrogen-mediated parasitic currents, thereby favoring more efficient borohydride electrooxidation. These observations indicate that Pt at ultralow loadings does not exhibit bulk-like electrochemical characteristics.

The voltammetric response of $Pt(NiCu)_{foam}/Ti$ in 0.05 M $NaBH_4$ + 1 M NaOH (Figure 6) shifts systematically toward more positive potentials from $Pt(NiCu)_{foam}/Ti$-1 to $Pt(NiCu)_{foam}/Ti$-3, accompanied by a significant increase in current density. This behavior is attributed to the progressive evolution of the Ni–Cu foam with increasing deposition time, which enhances Pt–NiCu interfacial site density and shifts the borohydride oxidation reaction from Ni–Cu framework-dominated behavior toward interfacial control with modified intermediate adsorption and reduced hydrogen adsorption/desorption contributions. The resulting change in adsorption–reaction balance requires slightly higher potentials for optimal kinetics, while the increased current confirms enhanced catalytic activity.

The high currents observed during the first voltammetric cycle on Pt-modified NiCu surfaces can be attributed to the activity of freshly exposed metallic Ni sites within the Ni–Cu foam scaffold. Subsequent cycles, show gradual current decline due to partial passivation of Ni through the formation of surface hydroxide/oxide species ($Ni(OH)_2/NiOOH$) and adsorption of reaction intermediates. Although repeated cycling leads to a current decline for both Pt-modified and unmodified catalysts, the decrease is less pronounced for Pt-modified coatings, particularly at higher Pt loadings, longer Ni–Cu deposition times, and especially at low potentials. The voltammetric profiles suggest that the electrodes evolve

toward a stable, catalytically favorable surface state rather than undergoing progressive deactivation, consistent with the tendency observed for unmodified $(NiCu)_{foam}/Ti$. The anodic features of the Pt-modified $(NiCu)_{foams}$ are primarily governed by Ni, which mediates sodium borohydride electrooxidation and influences hydrogen and OH^- adsorption on Pt surfaces, mitigating hydrogen accumulation [33,82]. Ultralow loading of Pt modifies the surface, facilitating the oxidation of reaction intermediates and contributing to the current density increase, while Cu further enhances performance by diluting hydrogen adsorption sites and tuning surface adsorption properties, suppressing hydrogen-related currents and improving overall BOR efficiency [60,62].

Increasing Pt loading from 9.63 to 19.04 μgPt cm^{-2} increases the first anodic peak current density by 1.16–2.83-fold compared to unmodified NiCu foams. This enhancement reflects the formation of an efficient ternary Ni–Cu–Pt catalytic system, in which ultralow Pt incorporation significantly boosts the intrinsic sodium borohydride electrooxidation activity of the NiCu framework. Notably, the $Pt(NiCu)_{foam}/Ti$ electrodes exhibit approximately eight-fold higher currents than bulk Pt under identical conditions, highlighting synergistic effect among Ni, Cu, and Pt and the efficient utilization of noble metal sites. Overall, CV results show that controlled surface modification by Pt significantly enhances the electrochemical response of bimetallic $(NiCu)_{foam}/Ti$ toward borohydride electrooxidation in alkaline media, as evidenced by higher current densities and more distinct voltammetric features compared with both bulk Pt and unmodified NiCu foams. Importantly, despite the ultralow Pt content and a total metal loading approximately half that of the unmodified foams, the ternary Ni–Cu–Pt system on a 3D porous Ni-rich bimetallic Ni–Cu foam scaffold delivers superior catalytic performance, combining the intrinsic activity of the Ni–Cu framework with synergistic Pt contributions. In addition, surface roughness and porosity act synergistically to govern the electrocatalytic performance of $Pt(NiCu)_{foam}/Ti$ and are co-optimized via the dynamic hydrogen bubble templating (DHBT) process, where deposition time and hydrogen evolution dynamics play key roles. Longer deposition times promote the formation of pronounced dendritic features, increasing surface roughness, while hydrogen bubble generation, growth, and detachment control pore size distribution and interconnectivity. The increased roughness is expected to enhance the exposure of catalytically active sites and promote BH_4^- adsorption and activation, whereas the porous architecture facilitates electrolyte penetration and reactant accessibility within the 3D structure. Together, these optimized features improve the accessibility of active sites within the Ni-rich NiCu framework and ultralow Pt species, maximizing their utilization and reinforcing their synergistic interaction. This results in enhanced borohydride electrooxidation activity and improved fuel cell performance compared to NiCu foam and bulk Pt.

These findings highlight Pt-modified bimetallic Ni–Cu foams as highly active, cost-effective catalysts for efficient alkaline borohydride electrooxidation, with the ternary system representing a key novelty in the design.

3.4. Fuel Cell Performance

The catalytic performance of the $(NiCu)_{foam}/Ti$ and $Pt(NiCu)_{foam}/Ti$ catalysts was further evaluated in a direct $NaBH_4$–H_2O_2 fuel cell using 1 M $NaBH_4$ + 4 M NaOH as the anolyte and 5 M H_2O_2 + 1.5 M HCl as the catholyte, separated by a Nafion N117 membrane. The cell exhibited an open-circuit voltage of approximately 1.9 V. Figure 7 presents the polarization and power density curves measured at temperatures between 25 and 55 °C for catalysts prepared at different synthesis times, corresponding to varying catalyst loadings.

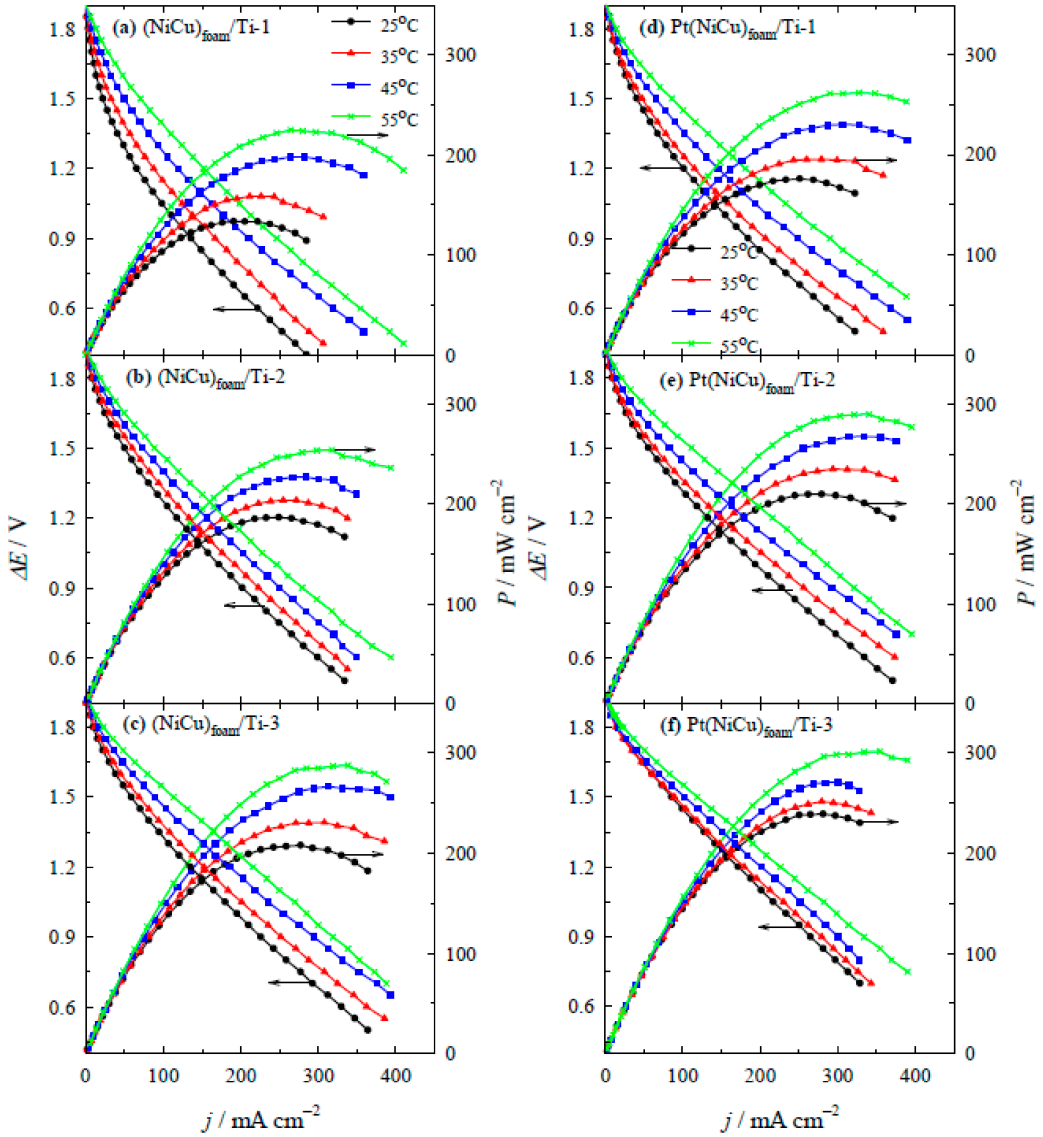


Figure 7. Cell polarization and corresponding power density curves of the $NaBH_4$-H_2O_2 fuel cell using $(NiCu)_{foam}$/Ti and $Pt(NiCu)_{foam}$/Ti catalysts as anodes at 25 °C (black line), 35 °C (red line), 45 °C (blue line), and 55 °C (green line). The anolyte consisted of 1 M $NaBH_4$ + 4 M NaOH, while the catholyte comprised 5 M H_2O_2 + 1.5 M HCl.

The performance parameters are summarized in Tables 2 and 3. In all cases, the $Pt(NiCu)_{foam}$/Ti anodes delivered significantly higher power densities than the unmodified NiCu foams, confirming the beneficial effect of Pt incorporation on the electrocatalytic activity toward sodium borohydride electrooxidation. For the $(NiCu)_{foam}$/Ti electrodes, increasing the temperature from 25 to 55 °C enhanced peak power density by 1.4–1.7-fold, whereas Pt-modified catalysts showed a 1.3–1.5-fold improvement.

The highest peak power density was obtained for Pt(NiCu)foam/Ti-3, reaching 239 mW cm^{-2} at 25 °C and increasing to 301.6 mW cm^{-2} at 55 °C, reflecting accelerated reaction kinetics and improved mass transport at elevated temperature.

The enhanced borohydride oxidation currents observed in cyclic voltammetry correlate well with the improved fuel cell performance, confirming that the synergistic Pt–NiCu catalytic interface effectively accelerates the anodic reaction under practical operating conditions, leading to more efficient Pt utilization. To further elucidate the role of Pt loading, a detailed analysis of its effect on catalytic performance is presented below.

Table 2. Main performance parameters of the DBHPFC at 25 °C using different anode foams.

Sample	Pt Loading, μg_{Pt} cm^{-2}	ΔE_{peak}, V	j_{peak}, mA cm^{-2}	P_{peak}, mWcm^{-2}	Specific P_{peak}, mW μg_{Pt}^{-1}
$(NiCu)_{foam}$/Ti-1	-	0.70	190.57	133.52	-
$(NiCu)_{foam}$/Ti-2	-	0.75	249.03	186.88	-
$(NiCu)_{foam}$/Ti-3	-	0.75	277.12	207.98	-
Pt$(NiCu)_{foam}$/Ti-1	9.63	0.70	251.16	175.90	18.27
Pt$(NiCu)_{foam}$/Ti-2	13.79	0.75	279.27	209.59	15.20
Pt$(NiCu)_{foam}$/Ti-3	19.04	0.85	281.15	239.14	12.56

Table 3. Main performance parameters of the DBHPFC at 55 °C using different anode foams.

Sample	Pt Loading, μg_{Pt} cm^{-2}	ΔE_{peak}, V	j_{peak}, mA cm^{-2}	P_{peak}, mWcm^{-2}	Specific P_{peak}, mW μg_{Pt}^{-1}
$(NiCu)_{foam}$/Ti-1	-	0.85	264.30	224.87	-
$(NiCu)_{foam}$/Ti-2	-	0.80	317.41	254.11	-
$(NiCu)_{foam}$/Ti-3	-	0.85	338.41	287.88	-
Pt$(NiCu)_{foam}$/Ti-1	9.63	0.80	327.38	262.02	27.21
Pt$(NiCu)_{foam}$/Ti-2	13.79	0.85	340.50	289.63	21.00
Pt$(NiCu)_{foam}$/Ti-3	19.04	0.85	354.52	301.60	15.84

A more detailed analysis of the Pt content effect reveals a non-linear relationship between Pt loading and catalytic performance. Increasing Pt loading from 9.63 to 19.04 μg cm^{-2} leads to a gradual increase in peak power density from 175.9 to 239.14 mW cm^{-2} at 25 °C and from 262.02 to 301.60 mW cm^{-2} at 55 °C, confirming the promoting role of Pt in enhancing borohydride oxidation under both operating temperatures. However, this improvement is not proportional to the Pt content. In contrast, the mass-specific activity decreases from 18.27 to 12.56 mW μgPt^{-1} at 25 °C and from 27.21 to 15.84 mW μgPt^{-1} at 55 °C with increasing Pt loading, clearly indicating diminishing returns in catalytic efficiency. This behavior demonstrates that the Ni–Cu foam framework provides the dominant contribution to overall catalytic activity, while Pt acts primarily as a surface promoter that enhances interfacial reaction kinetics. Notably, the highest Pt utilization efficiency is achieved at the lowest Pt loading, where finely dispersed Pt species maximize the accessibility of active sites. From a cost–performance perspective, these results highlight that ultralow Pt incorporation is sufficient to achieve high catalytic performance, while further increases in Pt content led to reduced utilization efficiency without proportional gains in activity.

The performance of the $NaBH_4$–H_2O_2 fuel cell using the Pt$(NiCu)_{foam}$/Ti anode developed in this study was compared with previously reported Ni-, Cu-, and Pt-based catalysts under various operating conditions, with the results summarized in Table 4. The Pt$(NiCu)_{foam}$/Ti anode exhibits maximum power densities ranging from 175 to 239 mW cm^{-2} at 25 °C (peak: 239 mW cm^{-2}) and 262–301 mW cm^{-2} at 55 °C (peak: 301.6 mW cm^{-2}). This corresponds to a 22% improvement over Ni@Pd/MWCNT (246.85 mW cm^{-2}) and a 126% increase over Ni@Pt/C (133.38 mW cm^{-2}), highlighting the significant enhancement achieved by the ternary Pt–Ni–Cu system.

Table 4. The comparison of DBHPFC performance using different electrocatalysts and anolytes-catholytes composition.

Anode	Cathode	Anolyte	Catholyte	P_{max}, mW cm^{-2}	T, °C	Ref.
NiMo/Ti-3	Pt	1 M $NaBH_4$ + 4 M NaOH	5 M H_2O_2 + 1.5 M HCl	33.0 46.6	25 55	-
Co-CoO@C/NF-600	Co-CoO@C-rGO/NF-600	0.4 M $NaBH_4$ + 2 M NaOH	0.5 M H_2O_2 + 2 M H_2SO_4	385.73	70	[15]
Ni_{50}-Co_{50}/rGO/NF	Pt/C 0.5 mg cm^{-2}	1 M $NaBH_4$ + 2 M NaOH	2 M H_2O_2 +0.5 M H_2SO_4	309	60	[16]
Pd/v-Ni_3S_2/NF	Pd/v-Ni_3S_2/NF	0.4 M $NaBH_4$ + 2 M NaOH	0.5 M H_2O_2 + 3 M NaOH	57.6 78	25 55	[17]
Pd/MoS_2/NiF	Pd/MoS_2/NiF	0.4 M $NaBH_4$ + 3 M NaOH	0.4 M H_2O_2 + 3 M NaOH	58.1 80.02	25 55	[18]
PdCu@rGOF	PdCu@rGOF	0.3 M $NaBH_4$ +2 M NaOH	1.3 M H_2O_2 + 2 M H_2SO_4	88.9 210.0	20 60	[19]
Ni@Pt/C	Pt/C	1 M $NaBH_4$ + 2 M NaOH	2 M H_2O_2 + 0.5 M H_2SO_4	47.66 133.38	25 60	[20]
Ni@Pd/MWCNT 1 mg cm^{-2}	Pt/C 0.5 mg cm^{-2}	1 M $NaBH_4$ + 2 M NaOH	2 M H_2O_2 + 0.5 M H_2SO_4	246.85	60	[21]
Pt mesh anode	Pt $Pt_{0.5}Ho_{0.5}$ $Pt_{0.5}Sm_{0.5}$	1 M $NaBH_4$ (98 wt.%, Scharlau) + 4 M NaOH	5 M H_2O_2 + 4 M NaOH	36 67 85	25	[22]
PtNi/C 1 mg cm^{-2}	Pt/C 0.5 mg cm^{-2}	1 M $NaBH_4$ + 2 M NaOH	2 M H_2O_2 +0.5 M H_2SO_4	106.63	60	[32]
Ni-np@NC (porous Ni–Cu alloy dendrite)	Pt/C	1 M $NaBH_4$ + 3 M NaOH	4 M H_2O_2 +1 M H_2SO_4	218	25	[60]
Ni@Pt/C	Pt/C 0.5 mg cm^{-2}	1 M $NaBH_4$ + 2 M NaOH	1 M H_2O_2 + 0.5 M H_2SO_4	68.64	60	[31]
$(NiCu)_{foam}$/Ti-1	Pt	4 M NaOH + 1 M $NaBH_4$	5 M H_2O_2 + 1.5 M HCl	133.52 224.87	25 55	[This work]
$(NiCu)_{foam}$/Ti-2	Pt	4 M NaOH + 1 M $NaBH_4$	5 M H_2O_2 + 1.5 M HCl	186.88 254.11	25 55	[This work]
$(NiCu)_{foam}$/Ti-3	Pt	4 M NaOH + 1 M $NaBH_4$	5 M H_2O_2 + 1.5 M HCl	207.98 287.09	25 55	[This work]
Pt$(NiCu)_{foam}$/Ti-1	Pt	4 M NaOH + 1 M $NaBH_4$	5 M H_2O_2 + 1.5 M HCl	175.92 262.02	25 55	[This work]
Pt$(NiCu)_{foam}$/Ti-2	Pt	4 M NaOH + 1 M $NaBH_4$	5 M H_2O_2 + 1.5 M HCl	209.59 289.63	25 55	[This work]
Pt$(NiCu)_{foam}$/Ti-3	Pt	4 M NaOH + 1 M $NaBH_4$	5 M H_2O_2 + 1.5 M HCl	239.14 301.6	25 55	[This work]

The high peak power density at moderate operating temperatures reflects both the intrinsic catalytic activity of the Pt–Ni–Cu system toward sodium borohydride electrooxidation and the beneficial role of the three-dimensional $(NiCu)_{foam}$/Ti architecture. When benchmarked against the literature reports, the Pt$(NiCu)_{foam}$/Ti catalyst surpasses most previously reported Ni- and Cu-based anodes as well as several noble-metal-modified electrodes. Although Co–CoO@C/NF-600 reports a higher peak power density (385.73 mW cm^{-2}), this was achieved at 70 °C, whereas the Pt$(NiCu)_{foam}$/Ti electrode attains comparable performance at 55 °C, demonstrating more efficient catalytic kinetics and mass transport under milder conditions.

Even high-performing electrodes such as Pd/V–Ni_3S_2/NF and Pd/MoS_2/NiF, which exhibit maximum power densities below 100 mW cm^{-2}, are clearly outperformed by the present catalyst.

Overall, this comparative analysis demonstrates that the $Pt(NiCu)_{foam}$/Ti anode is among the most competitive and high-performing DBHPFC anodes reported to date, particularly under practical, moderate-temperature conditions. The combination of the 3D foam architecture with the ternary Pt–Ni–Cu composition ensures high intrinsic activity and efficient Pt utilization, highlighting the potential of this electrode design for efficient and practical $NaBH_4$–H_2O_2 fuel cell applications.

4. Conclusions

Hierarchically porous, Ni-rich bimetallic Ni–Cu foams were successfully developed as an advanced architecture on Ti substrates via the dynamic hydrogen bubble templating method, followed by modification with ultralow Pt loading to construct a ternary Ni–Cu–Pt electrocatalytic system. The rational design delivers high catalytic activity toward sodium borohydride oxidation while minimizing precious metal usage. The dendritic morphology and interconnected three-dimensional pore network of the NiCu foam were tuned by controlling deposition time, enabling uniform metal distribution throughout the bimetallic framework. Compositional analysis confirmed Ni as the dominant component (28.09–34.61 mg cm^{-2}), forming a Ni-rich NiCu network, while Pt loading remained at ultralow levels (9.63–19.04 μg cm^{-2}), maximizing noble metal efficiency.

Electrochemical measurements demonstrated that bimetallic NiCu foams exhibit intrinsic borohydride oxidation activity, which is substantially enhanced upon Pt incorporation. In contrast to widely studied monometallic foams, the presence of Cu within the Ni framework creates a tunable bimetallic platform, improving selectivity and enabling synergistic interactions with the ultralow Pt promoter. Notably, despite nearly halving overall catalyst loading, the $Pt(NiCu)_{foam}$/Ti electrodes deliver approximately threefold higher oxidation currents compared to the unmodified NiCu foam and significantly outperforms bulk Pt. This enhanced catalytic performance originates from a strong synergistic interaction between the NiCu framework and ultralow Pt loading, which enhances borohydride oxidation at highly suppressed hydrogen related feature and sodium borohydride hydrolysis.

A systematic analysis of Pt loading further revealed a non-linear relationship between Pt content and catalytic performance. Although increasing Pt loading enhances absolute power density, the improvement is not proportional and is accompanied by a decrease in mass-specific activity at both 25 and 55 °C. This behavior clearly indicates diminishing returns at higher Pt loadings and identifies ultralow Pt incorporation as the most efficient regime for maximizing noble metal utilization and achieving an optimal cost–performance balance.

When implemented as anodes in $NaBH_4$–H_2O_2 fuel cells, the $Pt(NiCu)_{foam}$/Ti catalyst achieves peak power densities of 239 mW cm^{-2} at 25 °C and 301.6 mW cm^{-2} at 55 °C. The enhanced electrocatalytic performance is attributed to the combined effects of the three-dimensional hierarchical foam architecture, high Ni content, homogeneous Cu distribution, and the ultralow Pt promoter, which together provide favorable conditions for sodium borohydride electrooxidation.

Overall, this work presents a scalable, cost-effective, and high-performance strategy for sodium borohydride-based fuel cells. The developed $Pt(NiCu)_{foam}$/Ti electrodes integrate advanced self-supported 3D architectures with minimal noble metal content and provide a practical pathway toward efficient alkaline direct sodium borohydride fuel cells, highlighting the potential of ternary Ni–Cu–Pt systems for sustainable energy conversion applications.

https://doi.org/10.3390/cryst16050283

Author Contributions: Conceptualization, L.T.-T. and A.B.; methodology, J.V.; validation, D.Š., Ž.M. and A.B.; formal analysis, L.T.-T., A.B. and D.Š.; investigation, Ž.M.; data curation, J.V.; writing—original draft preparation, A.B. and D.Š.; writing—review and editing, L.T.-T. and E.N.; visualization, Ž.M., D.Š. and A.B.; supervision, L.T.-T.; project administration, E.N.; funding acquisition, L.T.-T. All authors have read and agreed to the published version of the manuscript.

Funding: This research was funded by the European Social Fund under Measure No. 09.3.3-LMT-K-712-19-0138 'Development of Competences of Scientists, other Researchers and Students through Practical Research Activities'.

Data Availability Statement: The original contributions presented in this study are included in the article. Further inquiries can be directed to the corresponding author.

Conflicts of Interest: The authors declare no conflicts of interest.

Abbreviations

The following abbreviations are used in this manuscript:

BOR	Sodium Borohydride Electrooxidation Reaction
DBFCs ($NaBH_4$–O_2)	Direct Borohydride Fuel Cells
DBHPFCs ($NaBH_4$–H_2O_2)	Direct Borohydride-Hydrogen Peroxide Fuel Cells
DHBT	Dynamic Hydrogen Bubble Templating Method
SEM	Scanning Electron Microscopy

References

1. Olabi, A.G.; Wilberforce, T.; Abdelkareem, M.A. Fuel cell application in the automotive industry and future perspective. *Energy* **2021**, *214*, 118955. [CrossRef]
2. Souza, F.M.; Pinheiro, V.S.; Gentil, T.C.; Lucchetti, L.E.B.; Silva, J.C.M.; Santos, M.L.M.G.; De Oliveira, I.; Dourado, W.M.C.; Amaral-Labat, G.; Okamoto, S.; et al. Advances in stationary and portable fuel cell applications. *J. Electroanal. Chem.* **2022**, *922*, 116712. [CrossRef]
3. Šljukić, B.; Santos, D.M.F. Direct borohydride fuel cells (DBFCs). In *Direct Liquid Fuel Cells*; Academic Press: Cambridge, MA, USA, 2021; pp. 203–232. [CrossRef]
4. Abahussain, A.A.M.; de León, C.P.; Arenas, L.F. The Direct Borohydride Fuel Cell. In *Encyclopedia of Electrochemistry*; Wiley: Hoboken, NJ, USA, 2021; pp. 1–35. [CrossRef]
5. Ma, J.; Choudhury, N.A.; Sahai, Y. A comprehensive review of direct borohydride fuel cells. *Renew. Sustain. Energy Rev.* **2010**, *14*, 183–199. [CrossRef]
6. Santos, D.M.F.; Sequeira, C.A.C. Sodium borohydride as a fuel for the future. *Renew. Sustain. Energy Rev.* **2011**, *15*, 3980–4001. [CrossRef]
7. Merino-Jiménez, I.; De León, C.P.; Shah, A.A.; Walsh, F.C. Developments in direct borohydride fuel cells and remaining challenges. *J. Power Sources* **2012**, *219*, 339–357. [CrossRef]
8. Oshchepkov, A.; Bonnefont, A.; Maranzana, G.; Savinova, E.R.; Chatenet, M. Direct borohydride fuel cells: A selected review of their reaction mechanisms, electrocatalysts, and influence of operating parameters on their performance. *Curr. Opin. Electrochem.* **2022**, *32*, 100883. [CrossRef]
9. Liu, L.; Zhang, J.; Zhao, Y.; Zhang, M.; Wu, L.; Yang, P.; Liu, Z. Research progress on direct borohydride fuel cells. *Chem. Commun.* **2024**, *60*, 1965–1978. [CrossRef]
10. Kojima, Y.; Haga, T. Recycling process of sodium metaborate to sodium, borohydride. *Int. J. Hydrogen Energy* **2003**, *28*, 989–993. [CrossRef]
11. Olu, P.-Y.; Job, N.; Chatenet, M. Evaluation of anode (electro)catalytic materials for the direct borohydride fuel cell: Methods and benchmarks. *J. Power Sources* **2016**, *327*, 235–257. [CrossRef]
12. Abdelhamid, H.N. A review on hydrogen generation from the hydrolysis of sodium borohydride. *Int. J. Hydrogen Energy* **2021**, *46*, 726–765. [CrossRef]
13. De Leon, C.P.; Walsh, F.C.; Rose, A.; Lakeman, J.B.; Browning, D.J.; Reeve, R.W. A direct borohydride–Acid peroxide fuel cell. *J. Power Sources* **2007**, *164*, 441–448. [CrossRef]
14. Sanli, A.E.; Gordesel, M.; Yilmaz, E.S.; Ozden, S.K.; Gunlu, G.; Uysal, B.Z. Performance improvement in direct borohydride/peroxide fuel cells. *Int. J. Hydrogen Energy* **2017**, *42*, 8119–8129. [CrossRef]

15. Gao, Y.; Meng, W.; Lv, Y.; Li, Y.; Geng, Z.; Niu, J.; Yao, J.; Yan, J.; Zhu, K.; Cao, D.; et al. In situ construction of Co-CoO heterostructures on rGO modified nickel foam for high-performance anode catalysts in direct borohydride-hydrogen peroxide fuel cells. *J. Energy Chem.* **2025**, *106*, 532–543. [CrossRef]
16. Mohamadi, T.; Hosseini, M.G.; Asadpour-Zeynali, K.; Majidi, M.R. High-performance direct borohydride-hydrogen peroxide fuel cell using Ni foam-supported Ni-Co nanoparticles as a noble-metal free anode electrocatalyst. *Synth. Met.* **2024**, *308*, 117729. [CrossRef]
17. He, W.; Wang, L.; Yin, D.; Wang, S.; Liu, H.; Yu, W.; Sun, L.; Dong, X. Nanoflower-like Pd/v-Ni_3S_2/Ni foam self-supporting electrode as bifunctional electrocatalyst for direct borohydride-hydrogen peroxide fuel cells. *Int. J. Hydrogen Energy* **2024**, *71*, 298–308. [CrossRef]
18. He, W.; Wang, L.; Yin, D.; Wang, S.; Liu, H.; Yu, W.; Sun, L.; Dong, X. Self-supporting honeycomb-like Pd/MoS_2/Ni foam electrode as a highly efficient bifunctional electrocatalyst for direct borohydride-hydrogen peroxide fuel cells. *J. Alloys Compd.* **2024**, *1007*, 176314. [CrossRef]
19. Yin, X.; Hou, M.; Zhu, K.; Ye, K.; Yan, J.; Cao, D.; Zhang, D.; Yao, J.; Wang, G. PdCu nanoparticles modified free-standing reduced graphene oxide framework as a highly efficient catalyst for direct borohydride-hydrogen peroxide fuel cell. *Renew. Energy* **2022**, *201*, 160–170. [CrossRef]
20. Hosseini, M.G.; Mahmoodi, R. Preparation method of Ni@Pt/C nanocatalyst affects the performance of direct borohydride-hydrogen peroxide fuel cell: Improved power density and increased catalytic oxidation of borohydride. *J. Colloid Interface Sci.* **2017**, *500*, 264–275. [CrossRef]
21. Hosseini, M.G.; Mahmoodi, R. Improvement of energy conversion efficiency and power generation in direct borohydride-hydrogen peroxide fuel cell: The effect of Ni-M core-shell nanoparticles (M = Pt, Pd, Ru)/Multiwalled Carbon Nanotubes on the cell performance. *J. Power Sources* **2017**, *370*, 87–97. [CrossRef]
22. Cardoso, D.S.P.; Santos, D.M.F.; Šljukić, B.; Sequeira, C.A.C.; Macciò, D.; Saccone, A. Platinum-rare earth cathodes for direct borohydride-peroxide fuel cells. *J. Power Sources* **2016**, *307*, 251–258. [CrossRef]
23. Santos, D.M.F.; Gomes, T.F.B.; Šljukić, B.; Sousa, N.; Sequeira, C.A.C.; Figueiredo, F.M.L. Perovskite cathodes for $NaBH_4/H_2O_2$ direct fuel cells. *Electrochim. Acta* **2015**, *178*, 163–170. [CrossRef]
24. An, L.; Zhao, T.; Yan, X.; Zhou, X.; Tan, P. The dual role of hydrogen peroxide in fuel cells. *Sci. Bull.* **2015**, *60*, 55–64. [CrossRef]
25. Balčiūnaitė, A.; Sukackienė, Z.; Tamašauskaitė-Tamašiūnaitė, L.; Vaitkus, R.; Norkus, E. Application of platinum–cobalt–boron as the anode material for sodium borohydride–hydrogen peroxide fuel cells. *Chemija* **2018**, *29*, 227–234. [CrossRef]
26. Zhang, D.; Sun, T.; Cao, D.; Liu, Y.; Jiao, W.; Wang, G. A review of anodes for direct borohydride fuel cells: Electrode and catalytic environment. *J. Power Sources* **2023**, *587*, 233684. [CrossRef]
27. Yusuf, B.A.; Yaseen, W.; Xie, J.; Babangida, A.A.; Muhammad, A.I.; Xie, M.; Xu, Y. Rational design of noble metal-based multimetallic nanomaterials: A review. *Nano Energy* **2022**, *104*, 107959. [CrossRef]
28. Lee, T.H.; Yu, S.S.; Oh, T.H. Effect of anode conditions on the performance of direct borohydride-hydrogen peroxide fuel cell system. *Int. J. Hydrogen Energy* **2023**, *48*, 18845–18855. [CrossRef]
29. Oh, T.H. Effect of cathode conditions on performance of direct borohydride-hydrogen peroxide fuel cell system for space exploration. *Renew. Energy* **2021**, *178*, 1156–1164. [CrossRef]
30. Oliveira, R.C.P.; Sevim, M.; Šljukić, B.; Sequeira, C.A.C.; Metin, O.; Santos, D.M.F. Mesoporous graphitic carbon nitride-supported binary MPt (M: Co, Ni, Cu) nanoalloys as electrocatalysts for borohydride oxidation and hydrogen evolution reaction. *Catal. Today* **2020**, *357*, 291–301. [CrossRef]
31. Hosseini, M.G.; Mahmoodi, R. The comparison of direct borohydride-hydrogen peroxide fuel cell performance with membrane electrode assembly prepared by catalyst coated membrane method and catalyst coated gas diffusion layer method using Ni@Pt/C as anodic catalyst. *Int. J. Hydrogen Energy* **2017**, *42*, 10363–10375. [CrossRef]
32. Hosseini, M.G.; Mahmoodi, R.; Amjadi, M.S. Carbon supported Ni_1Pt_1 nanocatalyst as superior electrocatalyst with increased power density in direct borohydride-hydrogen peroxide and investigation of cell impedance at different temperatures and discharging currents. *Energy* **2017**, *131*, 137–148. [CrossRef]
33. Guo, Y.; Hu, Z.; Cao, Y.; Tan, Q.; Yang, D.; Che, Y.; Zhang, C.; Ming, P.; Xiao, Q. Boosting borohydride oxidation kinetics by manipulating hydrogen evolution and oxidation through octahedral Pt–Ni/C for high-performance direct borohydride fuel cells. *J. Power Sources* **2024**, *612*, 234786. [CrossRef]
34. Martins, M.; Bozkurt, G.; Bayrakçeken, A.; Soylu, G.S.P.; Šljukić, B.; Santos, D.M.F. Pt-decorated binary transition metal oxides (MnO-NiO, MnO-TiO_2) for enhanced electrocatalysis of oxygen reduction and borohydride oxidation. *Mater. Sci. Eng. B* **2024**, *310*, 117745. [CrossRef]
35. Yi, L.; Wei, W.; Zhao, C.; Yang, C.; Tian, L.; Liu, J.; Wang, X. Electrochemical oxidation of sodium borohydride on carbon supported Pt-Zn nanoparticle bimetallic catalyst and its implications to direct borohydride-hydrogen peroxide fuel cell. *Electrochim. Acta* **2015**, *158*, 209–218. [CrossRef]

36. Balčiūnaitė, A.; Zabielaitė, A.; Upskuviene, D.; Tamašauskaitė-Tamašiūnaitė, L.; Stalnionienė, I.; Naruškevičius, L.; Vaičiūnienė, J.; Selskis, A.; Juškėnas, R.; Norkus, E. Platinum nanoparticles modified copper/titanium electrodes as electrocatalysts for borohydride oxidation. *Materials* **2021**, *14*, 7663. [CrossRef]
37. Liu, J.; Zhao, Q.; Chen, S.; Yi, L.; Wang, X.; Wei, W. Nanoporous carbon supported platinum-copper nanocomposites as anode catalysts for direct borohydride-hydrogen peroxide fuel cell. *Electrochim. Acta* **2015**, *171*, 96–104. [CrossRef]
38. Samad, S.; Loh, K.S.; Wong, W.Y.; Lee, T.K.; Sunarso, J.; Chong, S.T.; Daud, W.R.W. Carbon and non-carbon support materials for platinum-based catalysts in fuel cells. *Int. J. Hydrogen Energy* **2018**, *43*, 7823–7854. [CrossRef]
39. Chaikittisilp, W.; Ariga, K.; Yamauchi, Y. A new family of carbon materials: Synthesis of MOF-derived nanoporous carbons and their promising applications. *J. Mater. Chem. A* **2013**, *1*, 14–19. [CrossRef]
40. Rey-Raap, N.; dos Santos-Gómez, L.; Arenillas, A. Carbons for fuel cell energy generation. *Carbon* **2024**, *228*, 119291. [CrossRef]
41. Oliveira, R.C.P.; Milikić, J.; Das, E.; Yurtcan, A.B.; Santos, D.M.F.; Šljukić, B. Platinum/polypyrrole-carbon electrocatalysts for direct borohydride fuel cells. *Appl. Catal. B Environ.* **2018**, *238*, 454–464. [CrossRef]
42. Martins, M.; Šljukić, B.; Sequeira, C.A.C.; Soylu, G.S.P.; Yurtcan, A.B.; Bozkurt, G.; Sener, T.; Santos, D.M.F. PtNi supported on binary metal oxides: Potential bifunctional electrocatalysts for low-temperature fuel cells? *Appl. Surf. Sci.* **2018**, *428*, 31–40. [CrossRef]
43. Ma, X.; Jing, Z.; Feng, C.; Qiao, M.; Xu, D. Research and development progress of porous foam-based electrodes in advanced electrochemical energy storage devices: A critical review. *Renew. Sustain. Energy Rev.* **2023**, *173*, 113111. [CrossRef]
44. Ashby, M.F.; Evans, T.; Fleck, N.A.; Hutchinson, J.W.; Wadley, H.N.G. *Metal Foams: A Design Guide*; Butterworth-Heinemann: Oxford, UK, 2000.
45. Du, R.; Jin, X.; Hübner, R.; Fan, X.; Hu, Y.; Eychmüller, A. Engineering self-supported noble metal foams toward, electrocatalysis and beyond. *Adv. Energy Mater.* **2020**, *10*, 1901945. [CrossRef]
46. Vesztergom, S.; Dutta, A.; Rahaman, M.; Kiran, K.; Montiel, I.Z.; Broekmann, P. Hydrogen bubble templated metal foams as efficient catalysts of CO_2 electroreduction. *ChemCatChem* **2021**, *13*, 1039–1058. [CrossRef]
47. Reda, Y.; Abdel-Karim, R.; Zohdy, K.M.; El-Raghy, S. Electrochemical behavior of Ni–Cu foams fabricated by dynamic hydrogen bubble template electrodeposition used for energy applications. *Ain Shams Eng. J.* **2022**, *13*, 101532. [CrossRef]
48. Mohanty, A.; Balasubramaniam, S.; Ramadoss, A. 3D-C-Fe_4N@NiCu/Metallic macroporous frameworks for binder-free compact hybrid supercapacitors with high areal capacities. *Electrochim. Acta* **2023**, *440*, 141707. [CrossRef]
49. Shi, Y.; Xue, J.; Yu, Y.; Liu, N.; Tang, C. Construction of binder-free 3-D porous NiMn LDH electrode materials for high performance asymmetric supercapacitors using dynamic hydrogen bubbles as template. *J. Alloys Compd.* **2024**, *970*, 172513. [CrossRef]
50. Abdel-Karim, R.; Reda, Y.; Zohdy, K.M.; Abdelfatah, A.; El-Raghy, S. Electrochemical Performance of Porous Ni-Cu Anodes for Direct Methanol Fuel Cells. *Int. J. Electrochem. Sci.* **2019**, *14*, 3035–3054. [CrossRef]
51. Cheng, K.; Cao, D.; Yang, F.; Zhang, D.; Yan, P.; Yin, J.; Wang, G. Pd doped three-dimensional porous Ni film supported on Ni foam and its high performance towards $NaBH_4$, electrooxidation. *J. Power Sources* **2013**, *242*, 141–147. [CrossRef]
52. Hassanizadeh, E.; Mirjalili, M.; Moayed, M.H.; Darband, G.B. Ultra-fast electrodeposition of dynamic hydrogen bubble template nickel sulfide on a porous copper layer as an electrocatalyst toward hydrogen evolution reaction. *Int. J. Hydrogen Energy* **2024**, *55*, 729–739. [CrossRef]
53. Qian, Y.; Hu, M.; Li, L.; Cao, S.; Xu, J.; Hong, J.; Liu, X.; Xu, J.; Guo, C. Dynamically assisted electrodeposition by hydrogen bubbles on carbonized wood: A NiFeCo nanoflower electrocatalyst for efficient hydrogen evolution. *Fuel* **2024**, *361*, 130653. [CrossRef]
54. Siwek, K.I.; Eugénio, S.; Santos, D.M.F.; Silva, M.T.; Montemor, M.F. 3D nickel foams with controlled morphologies for hydrogen evolution reaction in highly alkaline media. *Int. J. Hydrogen Energy* **2019**, *44*, 1701–1709. [CrossRef]
55. Eugénio, S.; Demirci, U.B.; Silva, T.M.; Carmezim, M.J.; Montemor, M.F. Copper-cobalt foams as active and stable catalysts for hydrogen release by hydrolysis of sodium borohydride. *Int. J. Hydrogen Energy* **2016**, *41*, 8438–8448. [CrossRef]
56. Yang, L.; Wang, L.; Xing, C.; Wang, C.; Chang, S.; Zhao, Z. Bubble-template assisted fast electrochemical deposition of 3-D ternary Ni-Cu-Co alloy as promising catalyst for electrochemical overall water splitting. *Fuel* **2024**, *357*, 129890. [CrossRef]
57. Zhang, Y.; Tian, X.; Han, J.; Zhang, X.; Gao, Y.; Naren, G.; Yang, Y. Synthesis of Cu-doped Ni-B amorphous alloy catalyst and its catalytic performance for BH_4^- oxidation. *Arab. J. Chem.* **2025**, *18*, 106059. [CrossRef]
58. Santos, D.M.F.; Eugénio, S.; Cardoso, D.S.P.; Šljukić, B.; Montemor, M.F. Three-dimensional nanostructured Ni–Cu foams for borohydride oxidation. *Russ. J. Phys. Chem. A* **2015**, *89*, 2449–2454. [CrossRef]
59. Vorms, E.A.; Suprun, E.A.; Nartova, A.V.; Kvon, R.I.; Oshchepkov, A.G. Electrodeposited NiCu nanoparticles for the borohydride oxidation reaction: Effect of Cu on the activity and stability of Ni upon surface oxidation. *Electrochim. Acta* **2022**, *433*, 141196. [CrossRef]
60. Hu, B.; Yu, J.; Meng, J.; Xu, C.; Cai, J.; Zhang, B.; Liu, Y.; Yu, D.; Zhou, X.; Chen, C. Porous Ni−Cu alloy dendrite anode catalysts with high activity and selectivity for direct borohydride fuel cells. *ACS Appl. Mater. Interfaces* **2022**, *14*, 3910−3918. [CrossRef]

61. Mishra, K.; Devi, N.; Siwal, S.S.; Thakur, V.K. Insight perspective on the synthesis and morphological role of the noble and non-noble metal-based electrocatalyst in fuel cell application. *Appl. Catal. B Environ.* **2023**, *334*, 122820. [CrossRef]
62. Cherstiouk, O.V.; Simonov, P.A.; Oshchepkov, A.G.; Zaikovskii, V.I.; Kardash, T.Y.; Bonnefont, A.; Parmon, V.N.; Savinova, E.R. Electrocatalysis of the hydrogen oxidation reaction on carbon-supported bimetallic NiCu particles prepared by an improved wet chemical synthesis. *J. Electroanal. Chem.* **2016**, *783*, 146–151. [CrossRef]
63. Hu, B.; Xie, Y.; Yang, Y.; Meng, J.; Cai, J.; Chen, C.; Yu, D.; Zhou, X. Lattice strain controlled Ni@NiCu efficient anode catalysts for direct borohydride fuel cells. *Dalton Trans.* **2023**, *52*, 12002–12009. [CrossRef]
64. Lee, S.A.; Yang, J.W.; Choi, S.; Jang, H.W. Nanoscale electrodeposition: Dimension control and 3D conformality. *Explorations* **2021**, *1*, 20210012. [CrossRef] [PubMed]
65. Guo, M.; Cheng, Y.; Yu, Y.; Hu, J. Ni-Co nanoparticles immobilized on a 3D Ni foam template as a highly efficient catalyst for borohydride electrooxidation in alkaline medium. *Appl. Surf. Sci.* **2017**, *416*, 439–445. [CrossRef]
66. Barua, S.; Balčiūnaitė, A.; Vaičiūnienė, J.; Tamašauskaitė-Tamašiūnaitė, L.; Norkus, E. High-efficiency borohydride oxidation and oxygen reduction on titanium-supported Au(NiMo) catalysts for alkaline fuel cells. *Chem. Phys. Impact* **2025**, *10*, 100827. [CrossRef]
67. Campos-Roldán, C.A.; González-Huerta, R.G.; Alonso-Vante, N. Experimental protocol for HOR and ORR in alkaline electrochemical measurements. *J. Electrochem. Soc.* **2018**, *165*, J3001–J3007. [CrossRef]
68. LeBarron, C.T.; Koczaja, A.M.; Reidell, A.C.; Stewart, M.O.; Hosseini, S. Silver−silver chloride reference electrode: Construction and performance in nitrogen-containing organic solvent. *ACS Electrochem.* **2026**. [CrossRef]
69. Vaiyadurai, V.; Sankarasubramanian, S. A stable aqueous silver/silver chloride reference electrode with an operational temperature window from 233 to 353 K for extreme environments and space applications. *Anal. Chem.* **2026**, *98*, 2692−2700. [CrossRef] [PubMed]
70. Djokić, S.S. Fundamentals of Electroless Deposition. In *Encyclopedia of Electrochemistry*; Elsevier Inc.: Amsterdam, The Netherlands, 2018; pp. 161–173. [CrossRef]
71. Caballero-Briones, F.; Artés, J.M.; Díez-Pérez, I.; Gorostiza, P.; Sanz, F. Direct observation of the valence band edge by in situ ECSTM-ECTS in p-type Cu_2O layers prepared by copper anodization. *J. Phys. Chem. C* **2009**, *113*, 1028–1036. [CrossRef]
72. Giri, S.D.; Sarkarz, A. Electrochemical study of bulk and monolayer copper in alkaline solution. *J. Electrochem. Soc.* **2016**, *163*, H252–H259. [CrossRef]
73. Giziński, D.; Brudzisz, A.; Lee, J.; Harishchandre, R.; Choi, J.; Stępniowski, W.J.; Ziegler, K.J. Exploring the impact of chelating agents on copper oxide layer formation and morphology. *Inorg. Chem.* **2025**, *64*, 7437−7449. [CrossRef]
74. Oshchepkov, A.G.; Braesch, G.; Bonnefont, A.; Savinova, E.R.; Chatenet, M. Recent advances in the understanding of nickel-based catalysts for the oxidation of hydrogen-containing fuels in alkaline media. *ACS Catal.* **2020**, *10*, 7043−7068. [CrossRef]
75. Hall, D.S.; Bock, C.; MacDougall, B.R. The electrochemistry of metallic nickel: Oxides, hydroxides, hydrides and alkaline hydrogen evolution. *J. Electrochem. Soc.* **2013**, *160*, F235–F243. [CrossRef]
76. Habibi, B.; Delnavaz, N. Electrooxidation of glycerol on nickel and nickel alloy (Ni–Cu and Ni–Co) nanoparticles in alkaline media. *RSC Adv.* **2016**, *6*, 31797–31806. [CrossRef]
77. Zhang, L.; Ye, C.; Li, X.; Ding, Y.; Liang, H.; Wang, G.Z.Y. CuNi/C nanosheet array based on a metal–organic framework derivate as a supersensitive non-enzymatic glucose sensor. *Nano Micro Lett.* **2018**, *10*, 28. [CrossRef]
78. Trasatti, S. Physical electrochemistry of ceramic oxides. *Electrochim. Acta* **1991**, *36*, 225–241. [CrossRef]
79. Conway, B.E. *Electrochemical Supercapacitors: Scientific Fundamentals and Technological Applications*; Kluwer Academic/Plenum Publishers: New York, NY, USA, 1999.
80. Obradovića, M.D.; Gojković, S.L. Challenges in determining the electrochemically active surface area of Ni-oxides in the oxygen evolution reaction. *J. Electroanal. Chem.* **2022**, *918*, 116479. [CrossRef]
81. Xie, Z.; Qu, W.; Fisher, E.A.; Fahlman, J.; Asazawa, K.; Hayashi, T.; Shirataki, H.; Murase, H. Capacitance determination for the evaluation of electrochemically active surface area in a catalyst layer of NiFe-layered double hydroxides for anion exchange membrane water electrolyser. *Materials* **2024**, *17*, 556. [CrossRef]
82. Oshchepkov, A.G.; Braesch, G.; Ould-Amara, S.; Rostamikia, G.; Maranzana, G.; Bonnefont, A.; Papaefthimiou, V.; Janik, M.J.; Chatenet, M.; Savinova, E.R. Nickel metal nanoparticles as anode electrocatalysts for highly efficient direct borohydride fuel cells. *ACS Catal.* **2019**, *9*, 8520−8528. [CrossRef]
83. Oshchepkov, A.G.; Braesch, G.; Rostamikia, G.; Bonnefont, A.; Janik, M.J.; Chatenet, M.; Savinova, E.R. Insights into the borohydride electrooxidation reaction on metallic nickel from operando FTIRS, on-line DEMS and DFT. *Electrochim. Acta* **2021**, *389*, 138721. [CrossRef]

Disclaimer/Publisher's Note: The statements, opinions and data contained in all publications are solely those of the individual author(s) and contributor(s) and not of MDPI and/or the editor(s). MDPI and/or the editor(s) disclaim responsibility for any injury to people or property resulting from any ideas, methods, instructions or products referred to in the content.